



# Study of graphene by proton rainbow scattering

M. Hadžijović<sup>a</sup> and M. Ćosić

Laboratory of Physics, “Vinča” Institute of Nuclear Sciences, National Institute of the Republic of Serbia, University of Belgrade, P. O. Box 522, 11001 Belgrade, Serbia

Received 2 March 2023 / Accepted 5 May 2023 / Published online 30 May 2023

© The Author(s), under exclusive licence to EDP Sciences, SIF and Springer-Verlag GmbH Germany, part of Springer Nature 2023

**Abstract.** We have studied the transmission of 5 keV protons through graphene. Proton dynamics was modeled by classical theory. Proton trajectories define a mapping of the set of initial proton positions to the set of scattering angles. Singularities of the Jacobian associated with the introduced mapping form curves known as the rainbow lines. The differential cross section is infinite along the rainbow lines, making the proton count significantly larger along the rainbow pattern. Hence, rainbows dominantly determine the shape and size of the angular distribution of transmitted protons. It was found that reorientation of the graphene with respect to the incident beam direction and deformation of the graphene crystal lattice induce the transformation of the proton rainbow pattern. We thoroughly studied the morphological properties of the proton rainbow pattern. It was shown that angular distribution and the corresponding rainbow pattern could be used to determine the covariance matrix of atomic thermal displacements and to characterize point defects present in graphene.

## 1 Introduction

The existence of two-dimensional materials has been a highly disputed topic over the last century. The decrease in the melting point of thin films with the reduction in film thickness supported the claims that two-dimensional materials are unstable and, therefore, cannot exist [1, 2]. Discovery of graphene in 2004 proved that two-dimensional materials can exist [3]. Graphene is composed of carbon atoms arranged in a planar honeycomb lattice. It has extraordinary properties and potential applications [4–8].

It was found that isolated graphene samples are not perfectly flat. The direction of the normal to the graphene surface varies by a couple of degrees, and its surface is rippled [9]. Thermal vibrations of graphene were studied experimentally by electron diffraction [10]. Variances of in-plane and out-of-plane atomic displacements were measured at room temperature. Found values are 15.2 and 104 pm<sup>2</sup>, respectively. Results presented in studies [9], 10 differ significantly. It was speculated that the influence of the substrate or the presence of impurities could be the cause of this discrepancy [10]. Monte Carlo simulations of graphene

thermal vibrations were also performed [11]. The average length of individual ripples of the graphene surface was found to be around 80 Å, which is in agreement with the results presented in the study [9]. On the contrary, the average height of the ripples was calculated to be around 0.7 Å, differing significantly from the results presented in the reference [9]. The incompatibility of results obtained by theoretical and experimental investigations of graphene thermal motion motivated the further study of this topic. The results presented in this paper could be helpful in developing a completely novel technique for studying the thermal motion of atoms in graphene-like crystals. The presence of structural defects often has a negative effect on the properties of two-dimensional crystals [12–15]. In some cases, lattice defects are desirable because of their positive effect on some material characteristics. Therefore, controlled implementation of defects could enable fine-tuning of the desired properties of two-dimensional crystals. Micro-Raman spectroscopy and high-resolution transmission electron microscopy are practical and often used techniques for characterizing crystal defects. However, classic Raman spectroscopy cannot distinguish some defect types [14, 16, 17]. High-resolution transmission electron microscopy can be used to characterize crystal structure defects with outstanding resolution. However, energetic electrons used in beams of transmission electron microscopes can degrade the crystal lattice. It is worth mentioning that analysis of the obtained images via

T.I.: Physics of Ionized Gases and Spectroscopy of Isolated Complex Systems: Fundamentals and Applications. Guest editors: Bratislav Obradović, Jovan Cvetić, Dragana Ilić, Vladimir Srećković and Sylwia Ptasinska.

<sup>a</sup>e-mail: [milivoje@vin.bg.ac.rs](mailto:milivoje@vin.bg.ac.rs) (corresponding author)

transmission electron microscopes is far from straightforward [18–20].

Therefore, available characterization techniques of atomically thin crystals are not without limitations. We have inspected the possibility of characterizing two-dimensional crystals by studying the proton *rainbow scattering*. The rainbow scattering effect arises when particles from adjacent subsets of the impact parameter plane scatter in the same subset of the scattering angle plane. Consequently, the differential cross-sectional diverges along curves called rainbows. The shape of these lines determines the morphological properties of a transmitted proton angular yield. It was found that the rainbow scattering effect occurs in the classical axial transmission of protons through a very thin Si crystal [21]. The effect was experimentally verified soon afterward [22]. It was theoretically demonstrated that the transmitted ion rainbow pattern could be used to determine a more accurate model of the interaction potential between incident ions and atoms constituting the crystal lattice [23]. A bundle of parallel carbon nanotubes effectively forms a series of parallel circular and triangular axial channels. It was theoretically shown that morphological properties of the transmitted proton rainbow pattern could be used to determine the radius and length of nanotubes [24] and the density of topological defects present in such a bundle [25]. We have investigated whether a similar morphological analysis of transmitted protons' angular yield could lead to the characterization of atomically thin crystals, such as graphene.

The plan of this paper is as follows. First, we present the constructed model for the interaction potential between protons and graphene. Then the theory of rainbow scattering and momentum approximation is introduced. Proton rainbow scattering is analyzed afterward. Angular distributions of protons transmitted through the perfect graphene sheet and corresponding rainbow patterns are analyzed afterward. Then, the dependence of angular yields and rainbow patterns on the model of thermal vibrations is analyzed. A study of rainbow patterns generated by protons transmitted through graphene with three different kinds of point defects is presented afterward. The subsequent discussion explains how the shape and size of the rainbow lines could be used to extract the covariance matrix of atomic vibrations and identify defect types present in the graphene sample.

## 2 Theory

### 2.1 The interaction potential

We have studied the transmission of a parallel proton beam through graphene. The energy of each incident proton is 5 keV. Our goal was to understand the relations between morphological aspects of transmitted proton angular yield and properties of the corresponding graphene. It is worth highlighting that we have

studied proton scattering in the transmission regime only. Consequently, the developed model is inapplicable for studying large-angle scattering processes, such as backscattering.

Interaction between graphene and incident proton was modeled as a sum of binary proton-carbon interaction potentials. If the initial energy of transmitting protons is set to 5 keV, proton-carbon interaction can be accurately modeled by: Ziegler–Biersack–Littmark's [26], Molière's [27] or Doyle–Turner's [28] approximation. Molière derived a simple analytical approximation of the interaction potential starting from the Thomas–Fermi statistical model of an atom, in which electrons are treated as a free gas. Ziegler–Biersack–Littmark and Doyle–Turner's models are both based on the Hartree–Fock model of an atom, making it suitable for modeling interactions between ions and atoms of small atomic numbers. Doyle–Turner's analytical expression has been used for modeling interactions between ions and carbon atoms forming nanotubes [29]. Ziegler–Biersack–Littmark's model is divergent. On the contrary, Doyle–Turner's approximation is a sum of Gaussian functions, making it suitable for numerical and analytical calculations as well. For these reasons, we have modeled proton-carbon interaction potential by Doyle–Turner's approximation:

$$V_{DT}(r) = \frac{\hbar^2}{4\sqrt{\pi}m_e} \sum_{k=1}^4 \frac{\alpha_k}{(\beta_k/16\pi^2)^{3/2}} \exp\left[-\frac{4\pi^2 r^2}{\beta_k}\right], \quad (1)$$

where  $r$  is the proton-carbon distance,  $\hbar$  is reduced Planck's constant,  $m_e$  is electron mass, while  $\alpha = (0.07307, 0.1951, 0.04563, 0.01247)$  nm and  $\beta = (0.369951, 0.112966, 0.028139, 0.003456)$  nm<sup>2</sup> are fitting parameters for proton-carbon interaction.

The interaction time between 5 keV protons and graphene is significantly shorter than the period of atomic thermal oscillations. This means that transmitted protons interact with static carbon atoms randomly displaced around respective equilibrium positions of the graphene lattice. Thermal vibrations of atoms can be modeled in the following way. The distribution of atomic displacements relative to the equilibrium position is given by multivariate normal distribution:

$$P_{th}(\mathbf{r}') = \frac{1}{\sqrt{(2\pi)^3 |\det \Sigma|}} \exp\left(-\frac{1}{2} \mathbf{r}'^T \Sigma^{-1} \mathbf{r}'\right), \quad (2)$$

where  $\Sigma$  stands for the covariance matrix of atomic displacements. The covariance matrix of atomic thermal vibrations can be calculated by the Debye theory [21, 30]. In this approach, atomic displacements are assumed to be isotropic, and the following expression gives the variance of atomic thermal displacements:

$$\sigma^2 = \frac{\hbar}{(M_c m_u k_B \Theta_D/3)^{1/2}} \left( \frac{\mathcal{D}_f(\Theta_D/T)}{\Theta_D/T} + \frac{1}{4} \right), \quad (3)$$

where  $M_c = 12.0107$  kg is carbon atomic weight,  $m_u = 1.6605 \times 10^{-27}$  is the universal atomic mass unit,  $\Theta_D = 2000$  K is the Debye temperature of diamond [31],  $k_B = 1.3806 \times 10^{-23}$  J/K is Stefan–Boltzmann’s constant,  $T$  is the graphene absolute temperature, and  $\mathcal{D}_f$  is the Debye’s function. At the temperature  $T = 300$  K, according to Eq. (3), the variance of carbon atomic displacements equals  $17.3663$  pm<sup>2</sup>. We will refer to this model of graphene as the *Debye graphene*. We performed molecular dynamics calculations to provide a more realistic model of atomic vibrations [31]. We modeled a graphene sheet by a rhombic supercell with periodic boundary conditions applied in the graphene plane and fixed boundary conditions applied in the normal direction. The obtained covariance matrix of atomic thermal displacements is

$$\Sigma = \text{diag}(\sigma_\rho^2, \sigma_\rho^2, \sigma_z^2) = \text{diag}(17.67, 17.67, 2619.10) \text{ pm}^2. \tag{4}$$

We modeled graphene nanoribbons [32] by a supercell combining periodic and fixed boundary conditions in two orthogonal planar directions and fixed boundary conditions in the normal direction. The obtained covariance matrix of atomic thermal displacements is

$$\Sigma = \text{diag}(\sigma_x^2, \sigma_y^2, \sigma_z^2) = \text{diag}(18.14, 35.45, 3698.18) \text{ pm}^2. \tag{5}$$

Thermally averaged proton-carbon interaction potential is obtained by integration of the Doyle–Turner’s potential (1) over the distribution of atomic displacements (2):

$$V_{th}(\mathbf{r}) = \int d^3 2r' V_{DT}(\mathbf{r} - 2r') P_{th}(2r'). \tag{6}$$

Obtained integral is analytically solvable. Thermally averaged proton-carbon interaction potential is:

$$V_{th}(\mathbf{r}) = \frac{Z_1 \hbar^2}{4\sqrt{\pi} m_e} \sum_{k=1}^4 \frac{\alpha_k^{DT}}{\sqrt{\left| \det\left(\frac{\beta_k^{DT}}{16\pi^2} \mathbf{I} + \frac{1}{2} \Sigma\right) \right|}} \exp\left[-\frac{1}{4} \mathbf{r}^T \left(\frac{\beta_k^{DT}}{16\pi^2} \mathbf{I} + \frac{1}{2} \Sigma\right)^{-1} \mathbf{r}\right], \tag{7}$$

where  $\mathbf{r}$  is the proton-carbon separation vector, and  $\mathbf{r}^T$  is transposed vector, and  $\mathbf{I}$  is the identity matrix,

The proton graphene interaction potential is modeled as the sum:

$$U(\mathbf{r}) = \sum_{n=1}^N V_{th}(\mathbf{r} - \mathbf{R}_n). \tag{8}$$

where  $\mathbf{r}$  is the proton position vector, and  $\mathbf{R}_n$  ( $n = 1, \dots, N$ ) are position vectors of carbon atoms that dominantly participate in the scattering process. In the case of perfect graphene, carbon atoms form a honeycomb lattice with primitive vectors  $\mathbf{a}_1 = l(-\sqrt{3}/2, 3/2, 0)$ , and  $\mathbf{a}_2 = l(\sqrt{3}/2, 3/2, 0)$ , where  $l = 0.144$  nm is the distance between two neighboring carbon atoms. Relative positions of carbon atoms that constitute repeating motifs relative to the center of the unit cell are given by vectors  $\mathbf{g}_1 = l(0, -1/2, 0)$ ,  $\mathbf{g}_2 = l(0, 1/2, 0)$ . It is worth mentioning that constructed proton-graphene interaction potential has a translational symmetry of a modeled graphene lattice. This means that each unit cell contributes equally to the overall angular distribution. This insight drastically reduced the time necessary to perform numerical calculations.

### 2.2 Rainbow scattering

The energy of the incident protons is set to 5 keV. The associated proton de Broglie wavelength of  $4.0476 \times 10^{-4}$  nm is negligible compared to the distance of adjacent carbon atoms in the graphene lattice. Hence diffraction effects can be neglected, and solutions of the classical equations of motion well approximate proton trajectories. According to the Ziegler–Biersack–Littmark theory of energy loss [26], the total proton energy loss and scattering angle dispersion due to interaction with electrons are small. It is worth emphasizing that the developed model does not describe an electron capture process. We have studied the scattering of the non-neutralized part of a transmitted beam only. Consequently a theoretical distribution calculated by this model of scattering and an experimentally measured distribution are mutually incomparable unless an electrostatic analyzer is implemented to ensure the detection of non-neutralized protons only. This remark is crucial since 5 keV proton neutralization probability is approximately 40%, which is non-negligible.

Let us define the coordinate system such that the z-axis coincides with the direction of the incident proton beam. The direction of the proton beam relative to the graphene surface normal is specified by polar and azimuthal angles  $\Theta$  and  $\Phi$ . Proton-graphene interaction potential  $U$  is defined by the expression (8). Proton trajectories are solutions to the equations of motion:

$$m\ddot{\mathbf{r}}(t) = -\nabla U[\mathbf{r}(t)], \tag{9}$$

where  $m$  is the proton mass,  $\nabla U[\mathbf{r}(t)]$  is the gradient of the interaction potential  $U$  in the proton position  $\mathbf{r}(t)$  at the time  $t$ ,  $\ddot{\mathbf{r}}(t)$  is the proton acceleration at the time  $t$ . If proton transmission is a single scattering process and proton scattering angles are sufficiently small, transmission can be accurately modeled by the *momentum approximation* [33]. Then scattering law reduces to

the closed form:

$$\theta = -\frac{1}{2E_k} \nabla_{\perp} \varphi(b_x, b_y), \quad (10)$$

where  $\varphi$  is the *reduced interaction potential* defined by the expression:

$$\varphi(b_x, b_y) = \int_{-\infty}^{+\infty} dz U(r(z)). \quad (11)$$

Let  $(v_x, v_y, v_z)$  be the velocity of a transmitted proton. The following expressions define proton scattering angles  $\theta_x$  and  $\theta_y$ :

$$\tan \theta_x = \frac{v_x}{v_z}, \quad \tan \theta_y = \frac{v_y}{v_z}. \quad (12)$$

The angular yield of transmitted protons  $Y(\theta_x, \theta_y)$  is the number of protons scattered in the element  $d\theta_x d\theta_y$  centered at the  $(\theta_x, \theta_y)$ . Proton impact parameter  $(b_x, b_y)$  is a projection of the initial proton position to the transverse, i.e.,  $(x, y)$  plane.

Proton trajectories define a mapping of the proton impact parameters to the set of proton scattering angles:

$$f_{(\Theta, \Phi)} : (b_x, b_y) \rightarrow (\theta_x, \theta_y), \quad (13)$$

$\Theta$  and  $\Phi$  are treated as parameters of the function  $f_{(\Theta, \Phi)}$ . For differential cross section holds the following approximation:

$$\sigma(b_x, b_y; \Theta, \Phi) \sim |\det \mathcal{J}_{(\theta_x, \theta_y)}(b_x, b_y)|^{-1}, \quad (14)$$

where  $\mathcal{J}_{(\theta_x, \theta_y)}(b_x, b_y)$  is the Jacobian matrix of the mapping (13).  $\sigma$  is infinite at points for which holds:

$$\det \mathcal{J}_{(\theta_x, \theta_y)}(b_x, b_y) = 0. \quad (15)$$

Singularities of  $\mathcal{J}_{(\theta_x, \theta_y)}(b_x, b_y)$  form curves in the impact parameter plane, which are called *rainbows in the impact parameter plane*. Images of these curves obtained by mapping (13) are called *rainbow lines*. It will be shown that, as singularities of the differential cross section, rainbows significantly influence the shape of the angular distribution of transmitted protons. A rainbow pattern in the case of momentum approximation is obtained by substituting expression (10) in Eq. (15), which leads to the following expression:

$$\frac{\partial^2 \varphi}{\partial b_x^2} \frac{\partial^2 \varphi}{\partial b_y^2} - \left( \frac{\partial^2 \varphi}{\partial b_x \partial b_y} \right)^2 = 0. \quad (16)$$

Momentum approximation provides an interesting geometrical interpretation of the rainbow pattern. Notice that reduced interaction potential  $\varphi$  defines a

surface over the  $(b_x, b_y)$  plane. The curvature of this surface is proportional to the determinant of the hessian matrix of a function  $\varphi$ , given in the lefthand side of the expression (16). Therefore, rainbows are zero curvature contours of a reduced potential  $\varphi$ .

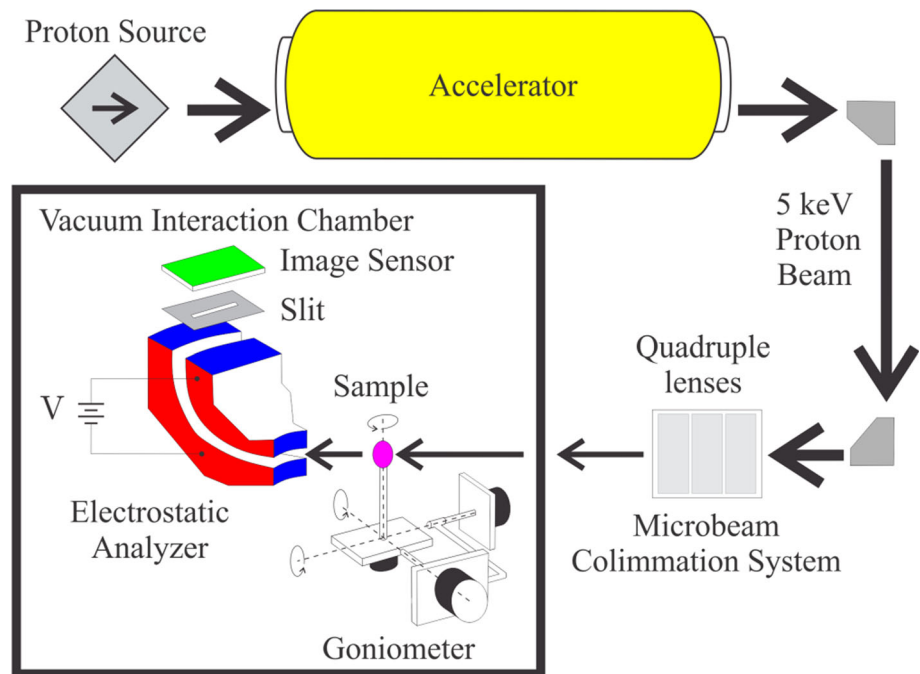
A study of crystal rainbows generated by protons transmitted through thin crystals could be helpful for the determination of a more accurate interaction potential [34, 35]. Theoretical investigation of the proton rainbow scattering on graphene revealed that the shape and size of the rainbow lines formed by protons strongly depend on the adopted interaction potential model [36]. This paper explores the possibility of studying graphene thermal vibrations and point defects by analyzing the rainbow pattern of transmitted protons.

### 3 Results and discussion

The first ever measured crystal rainbows were generated by the 7 MeV proton beam transmitted through a Si crystal's 198 nm long 110 channels [21]. A crystal rainbow pattern is observed in the measurements of the angular distributions of 2 MeV protons transmitted through 55 nm thick Si crystal [23]. The following experimental setup is proposed for the measurement of proton rainbow scattering on graphene.

We assume the graphene sample is a single sheet of the perfect freestanding graphene situated on top of the high-quality TEM grid [32]. The experimental setup required to measure the graphene rainbow patterns is presented in Fig. 1. It consists of a proton source, an accelerator, a collimation system, an interaction chamber containing a sample holder with a goniometer, an angularly resolved electrostatic analyzer, a microchannel plate amplifier, and an image acquisition system [32, 37, 38]. The experiment must be performed in a high vacuum to prevent energy and angular distortion of the proton beam caused by transport lines and to have a target as clean as possible [32, 37].

The collimation system and the electrostatic analyzer are essential for the successful measurement of the proton rainbow pattern. The transmitted proton's exiting position is proportional to the scattering angle. Microchannel plate provides spatial information and amplification of signals generated by transmitted protons. Electrostatic analyzer exclusively permits passage of particles with certain charge, hence enabling the distribution of non-neutralized protons to be measured solely. Proton beam angular divergence influences the measured image's sharpness. To observe the rainbow's dark side to bright side transition in the measured proton angular distributions, collimation of the proton beam is necessary. The width of this transition is approximately 1 mrad. Therefore, the detector of this resolution should be able to measure proton rainbow patterns [38–41].

**Fig. 1** Scheme of the experimental setup

### 3.1 Proton rainbow scattering

This section presents angular distributions of protons transmitted through the graphene sheet for different relative orientations of the graphene surface and the incident beam. Graphene sheet thermal vibrations are modeled by the covariance matrix (4). All results will be presented in the transverse plane of the incident beam. Particle counts will be expressed in the logarithmic scale.

Calculated angular distributions of protons transmitted through graphene sheet for zero azimuthal angle  $\Phi$  and values of the polar angles  $\Theta = 0$ ,  $\Theta = 600$  mrad, and  $\Theta = 900$  mrad, are presented in Fig. 2a–c, respectively. In the case of the normal incidence  $\Theta = 0$ , the outer part of the distribution has a circular shape. It is formed by protons that scatter in the vicinity of individual carbon atoms and reflects the spherical symmetry of a potential in these regions of space. The inner part of the distribution has a hexagonal shape, which reflects the symmetry of the reduced potential relative to the center of the graphene hexagon. Figure 2a' is the enlarged view of the central part of the angular plane. In the case of a sample tilted by the  $\Theta = 600$  mrad, the inner part of the distribution stretches along the vertical direction, and the outer part splits into two overlapping elliptical areas. In Fig. 2c inner part is composed of two triangular regions, while the outer part has an ellipse-like shape.

Solid black and purple lines in Fig. 2 are rainbow lines calculated by solving Eqs. (15) and (16), respectively. In both cases, the rainbow pattern in Fig. 2a has two parts. The inner part of the rainbow pattern is made of a single hexagonal line. Black and purple outer rainbows are circular lines of different diameters. The black

rainbow outlines the distribution perfectly. The diameter of the purple line is larger by 10.24%. If the tilt angle is  $\Theta = 600$  mrad, the inner rainbow gets stretched in the vertical direction. As in the case of the normal incidence, the black and purple lines are indistinguishable and outline the shape of the inner part of the distribution perfectly. In this case, the outer rainbow pattern is composed of two elliptic curves. Proton rainbow scattering on two carbon atoms forming a graphene unit cell generates two outer rainbows [37, 38]. Black and purple outer rainbows differ by the less amount than in the case of the normal incidence. In the case of  $\Theta = 900$  mrad, the inner part of the rainbow pattern consists of two triangular lines and one ellipse-like line. Black and purple lines are practically indistinguishable from each other. The momentum approximation can provide a very accurate model of proton-graphene scattering if scattering angles are sufficiently small. Figure 2 demonstrates that angular yield is significantly larger along the rainbow lines. In that sense, the rainbow pattern determines the shape and size of the angular distribution of transmitted protons.

The momentum approximation provides an understanding of the observed rainbow pattern transformation from a topological perspective. Reduced interaction potential  $\varphi$  is an integral of the interaction potential along the  $z$ -axis, making it dependent on the proton beam incident direction. Reduced potential maxima coincide with transverse atomic projections. In the case of a normal incidence, at the center of a unit cell is a global minimum of the function  $\varphi$ , surrounded by six of its maxima. Hence, for topological reasons, the surface associated with the function  $\varphi$  must have at least one zero curvature contour encircling the central minimum. The regular arrangement of six potential maxima around the center of a unit cell imposes hexagonal

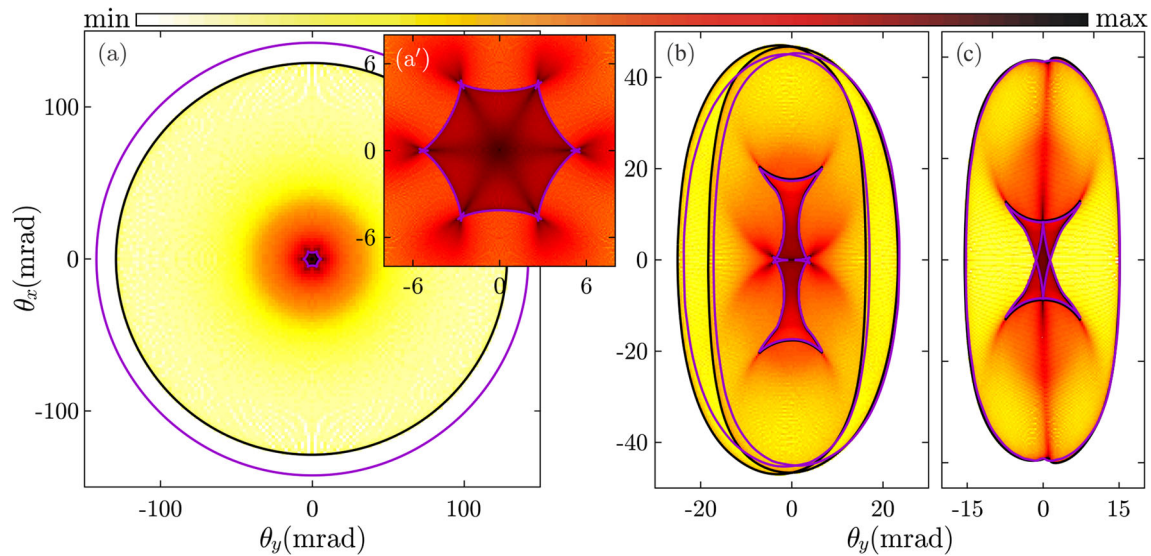


**Fig. 2** a–c Angular distributions of 5 keV protons transmitted through graphene with  $\Sigma = \text{diag}(17.67, 17.67, 2619.10)$  pm<sup>2</sup>, tilted for  $\Theta = 0, 600,$  and  $900$  mrad, respectively. The inset (a') shows an enlarged view of the distributions in the vicinity of the coordinate origin. Black and purple lines are rainbow lines obtained by solving equations of motion and momentum approximation, respectively. The associated color map shows the relative yield levels

symmetry on this curve. Scattering law (10) maps this zero curvature contour to the purple rainbow line visible in Fig. 2a'. Tilting graphene changes atomic transverse projections, which breaks the reduced potential's hexagonal symmetry and transforms the inner rainbow line. The inner rainbow's most abrupt change is splitting into two rainbows, observable in Fig. 2b. This process reflects a bifurcation of the reduced potential central minimum into two minima [42].

Reduced potential maxima are surrounded by zero curvature contours, each giving rise to one outer rainbow line. Sufficiently close to the individual carbon atoms, reduced proton-graphene interaction potential is indistinguishable from the reduced proton-carbon interaction potential. Notice that proton-carbon interaction potential (7) is not spherically symmetric since atomic thermal vibrations are not isotropic. Suppose that the proton beam incidence direction is normal to the graphene surface. The integral of potential (7) along the beam incidence direction has circular symmetry since the associated covariance matrix is given by expression (4). Therefore, the zero curvature contour surrounding the potential's maximum has to be circular. Since the graphene unit cell is diatomic, there are two such curves, each surrounding one transverse atomic projection. From the symmetry standpoint, these two "atomic" zero curvature contours have to be nearly identical in the normal incidence case. The scattering law (10) maps these two curves into a single circular outer rainbow line in Fig. 2a. For tilted graphene, reduced proton-carbon interaction potential does not have a circular symmetry, which is reflected in the shape of the associated outer rainbow lines. The merging of two outer rainbows into a single rainbow line observed

in Fig. 2 is explained as follows. As graphene tilts, transverse positions of two adjacent carbon atoms approach each other. Eventually, two associated reduced potentials' maxima bifurcate into one, leading to a single outer rainbow line in Fig. 2c [42].

The outer rainbow line might seem to be an artifact of the thermal averaging procedure (6). To demonstrate that it is not the case, we have analyzed proton angular yields corresponding to static graphene. For simplicity, scattering was modeled by the momentum approximation. Proton-carbon interaction potential is modeled by the expression (1). Obtained angular proton yield in the normal incidence case is presented in Fig. 3a. The distribution is enclosed by the circular rainbow line  $C$ . The yield cross section in the relevant interval of scattering angles is presented in Fig. 3b. The position of the rainbow line is marked by the purple arrow and labeled by the letter  $C$ . Particle count is zero outside the region enclosed by the outer rainbow line  $C$ .

Therefore, the existence of the outer rainbow line is not predicated on the thermal averaging procedure. Sufficiently close to the individual carbon atoms proton-graphene interaction potential is well approximated by the Doyle-Turner's proton-carbon interaction, i.e., by a sum of Gaussian functions. Hence, the reduced proton-carbon interaction potential has a zero curvature contour which generates a rainbow line according to the expression (16). This feature of the Doyle-Turner's approximation reflects a screening effect. Therefore, the presented results are valid as much as the applied Doyle-Turner's approximation is accurate. We acknowledge that it is an open question whether a similar large-angle rainbow line exists in the case of other models of interatomic potential. However, it lies beyond the scope of the carried investigation. The presented

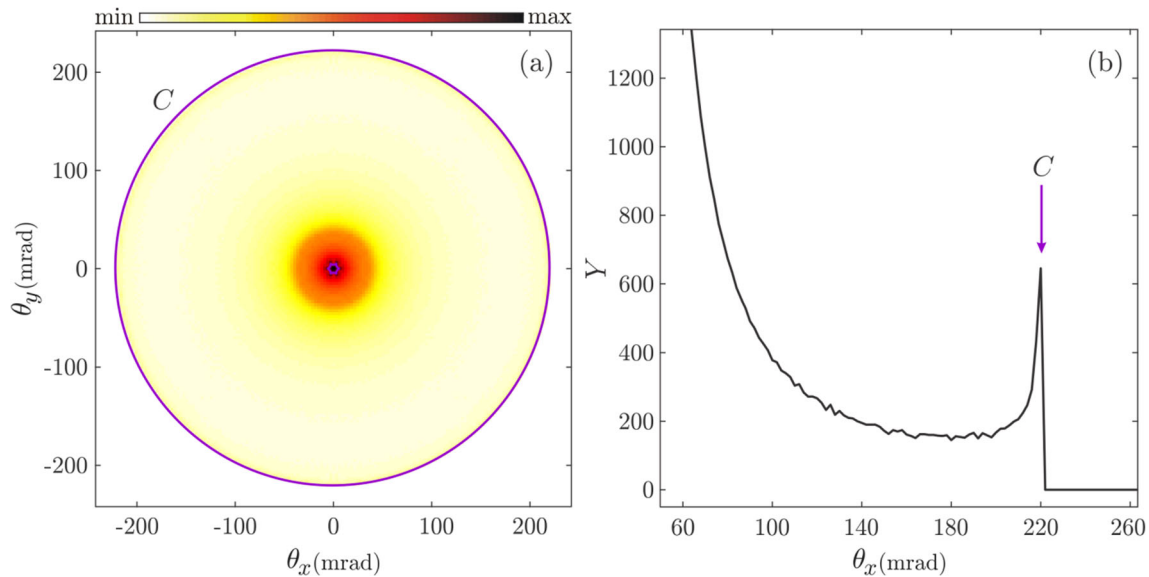


**Fig. 3** **a** Angular distribution of 5 keV protons transmitted through static graphene in the case of normal incidence. Corresponding rainbow pattern is presented by purple lines. The associated color map shows the relative yield levels. **b** Particle count  $Y$  as a function of scattering angle  $\theta_x$ . Purple arrow marks the position of the rainbow line  $C$

research aims to demonstrate how the morphological analysis of rainbow patterns could be used to characterize two-dimensional crystals.

### 3.2 Graphene thermal vibrations and proton rainbow scattering

First, we will study angular distributions and corresponding rainbow patterns generated by 5 keV proton beam transmission through perfect graphene with different covariances of atomic thermal vibrations. We analyzed proton rainbow scattering on the Debye graphene, graphene sheet, and graphene nanoribbons. Covariances of the respective graphene models are given by the expressions (3)–(5). As in the previous section, all results are presented in the transverse plane of the proton beam. Proton count is expressed in the logarithmic scale and presented by the associated colormap.

The angular distribution of protons transmitted through the Debye graphene in the case of the normal incidence and sample tilted by the angle  $\Theta = 0.065\pi$  rad are presented in Fig. 4a', a'', respectively. Distribution in the case of the sample tilted and rotated by the angles  $\Theta = 0.065\pi$  rad and  $\Phi = 0.25\pi$  rad is shown in Fig. 4a'''. Insets of these figures represent enlarged views of the central regions of the corresponding angular yields. Solid black lines in Fig. 4a', a'', and a''' are rainbow lines calculated by solving Eq. (15). The particle count is significantly larger along the rainbow lines. As expected, the rainbow pattern determines the shape and size of the angular distribution. In all considered cases, a rainbow pattern is composed of the outer and the inner rainbow. Outer rainbows  $O'_1$ ,  $O''_1$ , and  $O'''_1$  are nearly identical circles of radii  $D_c = 305.27$  mrad,

$D_c = 305.29$  mrad, and  $D_c = 305.25$  mrad, respectively. Note that the outer rainbow is circular regardless of the direction of the incident beam [31]. On the contrary, the rainbow pattern's inner part changes with the graphene's reorientation. Inner rainbows  $I'_1$ ,  $I''_1$  and  $I'''_1$  have hexagonal symmetry. In each vertex point of line  $I_1$  three singular points form a pattern known as the butterfly. It was shown that the transformation of the inner rainbow  $I_1$  is qualitatively equivalent to the transformation of the graphene hexagon transverse projection due to the graphene reorientation [31].

The angular distribution of protons transmitted through the graphene sheet in the normal incidence case and sample tilted by the angle  $\Theta = 0.065\pi$  rad are presented in Fig. 4b', b'', respectively. Distribution in the case of the sample tilted and rotated by the angles  $\Theta = 0.065\pi$  rad and  $\Phi = 0.25\pi$  rad is shown in Fig. 4b'''. Solid black lines in Fig. 4b', b'', and b''' are rainbow lines calculated by solving Eq. (15). Particle count is significantly larger along the calculated rainbow lines, which outline the entire distribution. The rainbow pattern is again composed of two parts: the outer rainbow and the inner rainbow. Outer rainbow  $O'_2$  is a circle of diameter  $D_c = 256.81$  mrad [31]. However, one can notice that, in the case of the graphene sheet, the circular shape of the outer rainbow is not conserved after the reorientation of the graphene. Blue horizontal and vertical lines in Fig. 4b'' and b''' are symmetry axes of the corresponding outer rainbows  $O'_2$  and  $O''_2$ . Major and minor cross sections of the rainbow  $O'_2$  along its symmetry axes are  $D_e^M = 196.21$  mrad and  $D_e^m = 153.04$  mrad, respectively. Major and minor cross sections of the rainbow  $O''_2$  along its symmetry axes are  $D_e^M = 196.05$  mrad and  $D_e^m = 153.03$  mrad, respectively. It was shown that inner rainbows

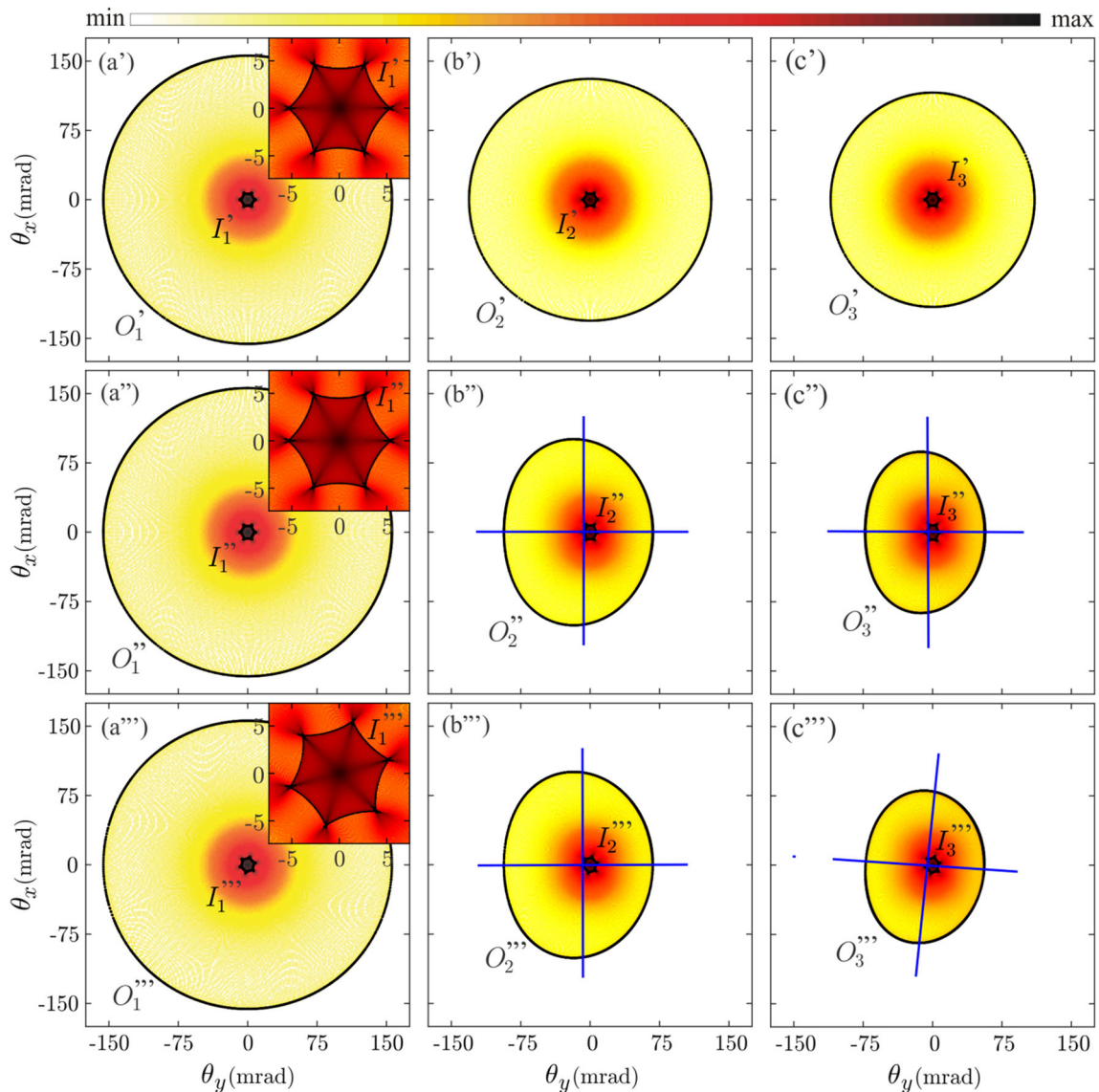


**Fig. 4** Angular yields of normal incident protons transmitted through Debye graphene, graphene sheet, and graphene nanoribbons are presented in figures **a'–c'**. Yields in the case of targets tilted by the angle  $\Theta = 0.065\pi$  rad are presented in figures **a''–c''**. Yields in the case of targets tilted by the angle  $\Theta = 0.065\pi$  rad and additionally rotated by  $\Phi = 0.25\pi$  rad are presented in figures **a'''–c'''**. Solid black lines are rainbow lines. Blue lines in figures **b'', c'', b''',** and **c'''** are symmetry axes of the corresponding outer rainbows. Proton count is expressed in the logarithmic scale and by the associated colormap

$I'_2$ ,  $I''_2$  and  $I'''_2$  are practically indistinguishable from the rainbows  $I'_1$ ,  $I''_1$  and  $I'''_1$ , respectively [31].

The angular distribution of protons transmitted through the graphene nanoribbon in the case of the normal incidence and sample tilted by the angle  $\Theta = 0.065\pi$  rad are presented in Fig. 4c' and c'', respectively. Angular proton distribution in the case of the sample tilted and rotated by the angles  $\Theta = 0.065\pi$  rad and  $\Phi = 0.25\pi$  rad is shown in Fig. 4c'''. Solid black lines in Fig. 4c', c'', and c''' are rainbow lines calculated by solving Eq. (15). Rainbows determine the shape of these distributions. Rainbow patterns are composed of two parts: the outer rainbow and the inner rainbow. Outer rainbow  $O'_3$  is an ellipse [31]. This ellipse's

major and minor diameters are  $D_e^M = 227.11$  mrad and  $D_e^m = 215.06$  mrad, respectively. Shape and size of the outer rainbow change with the reorientation of the graphene nanoribbon. Its symmetry axes are parallel with the vertical and horizontal directions. The major and minor diameters of rainbow  $O''_3$  are  $D_e^M = 165.11$  mrad and  $D_e^m = 121.26$  mrad. Additional rotation by the angle  $\Phi = 0.25\pi$  rad, outer rainbow tilts. Blue mutually orthogonal lines in Fig. 4c''' are symmetry axes of the rainbow  $O'''_3$ . Its major and minor cross-sections along the symmetry axes are  $D_e^M = 160.36$  mrad and  $D_e^m = 120.01$  mrad, respectively. It was shown that the inner rainbow  $I'_3$  is practically identical to the rainbow  $I'_2$ , making it indistinguishable



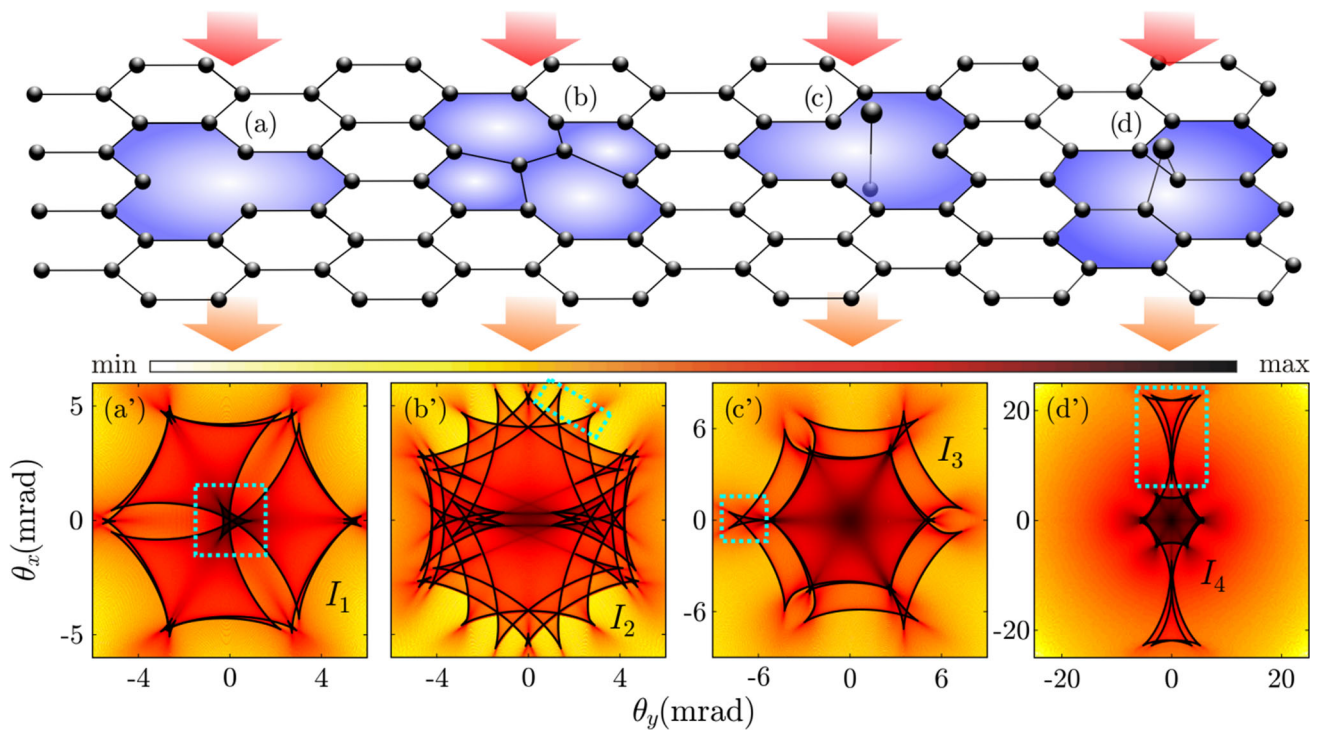


**Fig. 5** Red and orange arrows present the incident and transmitted proton beam, respectively. Black spheres are carbon atoms. **a–d** are depictions of vacancy, Stone–Wales defect, adatom defect and adatom in the bridge-like configuration defect, respectively. Corresponding angular distributions of the transmitted normal incident proton beam are presented in figures **a’–d’**. Black lines represent rainbows. Dashed cyan lines enclose characteristic segments of the corresponding rainbow patterns. Angular yield is expressed in the logarithmic scale and presented by the associated colormap

from the line  $I'_1$ . Similarly holds  $I'_3 = I'_2 = I'_1$ , and  $I'''_3 = I'''_2 = I'''_1$  [31].

From the previous paragraphs, one can conclude that the shape and size of the inner rainbow line, and therefore the shape of the inner part of the angular proton yield, do not depend on the covariance matrix of atomic thermal vibrations. This can be explained in the following way. Inner lines are formed by the synergic action of all carbon atoms that constitute the graphene hexagon. Protons that form inner rainbows scatter sufficiently far from the carbon atoms in the regions where thermal vibrations of individual atoms have an insignificant influence on the scattering process. However, the inner rainbows' shape depends on the relative orientation of the crystal and proton beam. Different crystal orientations have different atomic transverse projections, generating different inner rainbow patterns. Hence, the inner rainbow pattern depends on the spatial distribution of carbon atoms, i.e., crystal structure. This claim will be explored further in the next section.

Outer rainbows depend strongly on the covariance of atomic thermal vibrations. The circular shape of the outer rainbow in the case of the Debye graphene, regardless of the incident beam direction, can be explained in the following way. An outer rainbow is formed by trajectories of those protons that scatter in the close vicinity of individual atoms. It was pointed out that in this region of space, due to the isotropic motion of carbon atoms, interaction potential has spherical

symmetry. Hence, regardless of the incident beam direction, protons effectively scatter in the spherical potential giving rise to the circular angular yield.

Similar arguments could be used to explain the shapes of all studied outer rainbows. An outer rainbow line can be modeled by an elliptical line which is qualitatively equivalent to a normal projection of the ellipsoid associated with the matrix  $\Sigma^{-1}$  [31]. In the case of the Debye graphene, the ellipsoid associated with the matrix  $\Sigma^{-1}$  is a sphere. Any projection of this sphere is a circle, and such are the corresponding outer rainbow lines  $O'_1, O''_1$ , and  $O'''_1$ . In the case of the graphene sheet, covariance is given by the matrix (4). Corresponding ellipsoid  $\Sigma^{-1}$  has equal semi-axes in the  $x$  and  $y$  direction. The transverse projection of this ellipsoid in the normal incidence case is a circle, and such is the shape of the corresponding rainbow  $O'_2$  in Fig. 4b'. Tilting the graphene sheet by the angle  $\Theta = 0.065\pi$  rad transforms the transverse projection of the ellipsoid  $\Sigma^{-1}$  into an ellipse. Qualitatively similar is the rainbow transformation  $O'_2 \rightarrow O''_2$ . Transverse projections of the ellipsoid  $\Sigma^{-1}$  are invariant under the additional azimuthal rotations, leaving the outer rainbow practically unchanged in Fig. 4b'''. Transformation of the rainbow  $O'_3$  can be explained in the same way. Covariance in the case of nanoribbons is given by the matrix (5). Corresponding ellipsoid  $\Sigma^{-1}$  has all semi-axes different. In the case of the normal incidence, the transverse projection of

ellipsoid  $\Sigma^{-1}$  is an ellipse. Tilting nanoribbons by the angle  $\Theta = 0.065\pi$  rad deforms transverse projections of the ellipsoid  $\Sigma^{-1}$ , leaving it oriented along the vertical and horizontal axes. Additional azimuthal rotation by the angle  $\Phi = 0.25\pi$  rad causes the additional tilt of the transverse projection. Rainbow  $O_3$  follows qualitatively equivalent transformation:  $O'_3 \rightarrow O''_3 \rightarrow O'''_3$  observed in Fig. 4c', c'' and c'''.

### 3.3 Graphene defects and proton rainbow scattering

In this section, we will study the influence of graphene defects on the angular distribution of transmitted protons and the corresponding rainbow pattern. There are three types of graphene point defects: vacancies, topological defects, and additional carbon atoms [13]. The removal of any carbon atom forms a vacancy. A structural defect characterized by the absence of a single atom is sometimes called *monovacancy*. *Divacancy* is formed by the removal of two adjacent carbon atoms or by the merging of two monovacancies. The rearrangement of graphene atoms forms topological defects. E.g., rotation of the atomic pair transforms four graphene hexagons into two pentagon-heptagon pairs. An obtained structural defect is often called *Stone–Wales* or 55–77 defect. A carbon–carbon pair rotation in the divacancy defect leads to the topological defect consisting of three graphene pentagons and three graphene septagons. This point defect is known as the 555–777 defect. The third class of graphene point defects is the presence of additional off-plane carbon atoms in the graphene lattice. There are two most stable such configurations. An additional carbon atom could be positioned right above the carbon–carbon bond in the so-called *bridge defect* configuration. The second stable position of the additional carbon is right on top of the graphene's carbon atom. This defect is known as *adatom*.

Structurally imperfect graphene can be modeled by periodic in-plane translation of the graphene segment containing at least one point defect. Such unit cell with the minimal possible area we named the *defect cell*. Areas of defect cells in the case of monovacancy, adatom, Stone–Wales, and bridge defect are  $S_d = 3S_u$ ,  $3S_u$ ,  $4S_u$  and  $4S_u$ , respectively. Note that in this approach, although imperfect, modeled defective graphene has a periodic crystal structure. Consequently, the constructed proton-graphene interaction potential has the translational symmetry of a modeled imperfect graphene lattice. Therefore, each defect cell contributes equally to the overall angular distribution.

The previous section demonstrated that the inner part of the rainbow pattern changes with the reorientation of the sample and therefore depends on the spatial distribution of graphene atoms relative to the beam direction. The rainbow pattern's inner part depends on the graphene lattice's structural properties. Hence, in this section, we will focus solely on the inner part of the angular yield and the corresponding inner rainbow pattern. The results in Fig. 2 demonstrate that the inner

part of the angular yield and the corresponding rainbow pattern's inner part can be accurately modeled by the momentum approximation. For this reason, all results presented in this section are obtained by the momentum approximation.

Figure 5 presents angular distributions and corresponding rainbow patterns generated by transmitted 5 keV proton beam through graphene with different point defects. Red and orange arrows indicate the incident and transmitted proton beam, respectively. Vacancy, Stone–Wales, carbon adatom, and carbon adatom in the bridge-like configuration defect are illustrated in Fig. 5a–d, respectively. Black spheres represent carbon atoms. Carbon–carbon bonds are presented by thin black lines connecting neighboring carbon atoms. Thermal vibrations of graphene atoms are modeled by the covariance matrix (4).

Corresponding angular distributions of transmitted protons in the case of normal incidence are presented in Fig. 5a'–d'. The densities of the modeled defects are maximal. Proton count is expressed in the logarithmic scale and presented by the associated colormaps. Blue transparent surfaces are drawn to highlight specific point defects. Solid black lines represent rainbow lines calculated by solving Eq. (16).

One can notice that rainbow patterns  $I_1$ ,  $I_2$ ,  $I_3$  and  $I_4$  outline the shape of calculated angular distributions. Pattern  $I_1$  is composed of four rainbow lines [43]. All four lines surround the coordinate origin of the scattering angle plane. Central rainbow has a cusped triangular shape. The other three rainbows are pentagonal lines with a cusp and butterfly pattern decorating their vertices. Pattern  $I_2$  is formed by two pentagonal and two heptagonal lines [43]. Each pentagonal line has two cusps, two butterfly patterns, and a wigwam pattern at its vertices. Septagonal lines have two cusp patterns and five butterfly patterns at their vertices. Pattern  $I_3$  is formed by three hexagonal lines elongated in directions  $\pi/3$ ,  $\pi$ , and  $5\pi/3$  [43]. Each of these three rainbows has one large and three smaller butterfly patterns and two cusp patterns at the vertices of the hexagons. Rainbow pattern  $I_4$  is formed by a hexagonal line, corresponding to the perfect graphene, and two symmetrically equivalent rainbows composed of two butterfly patterns and seven cusps.  $\theta_x$  and  $\theta_y$  axes are the symmetry axes of the rainbow pattern  $I_4$ . Rainbow pattern  $I_4$  stretches furthest in the vertical direction and is significantly larger than patterns  $I_1$ ,  $I_2$ , and  $I_3$ .

## 4 Characterization of graphene by the rainbow scattering pattern

### 4.1 Extraction of the covariance matrix

This section will demonstrate how the covariance matrix of graphene atomic displacements could be extracted from the parameters of the outer rainbow line. From the results presented in Fig. 4, it is evident that the outer part of the rainbow pattern contains information about the spectrum of the covariance

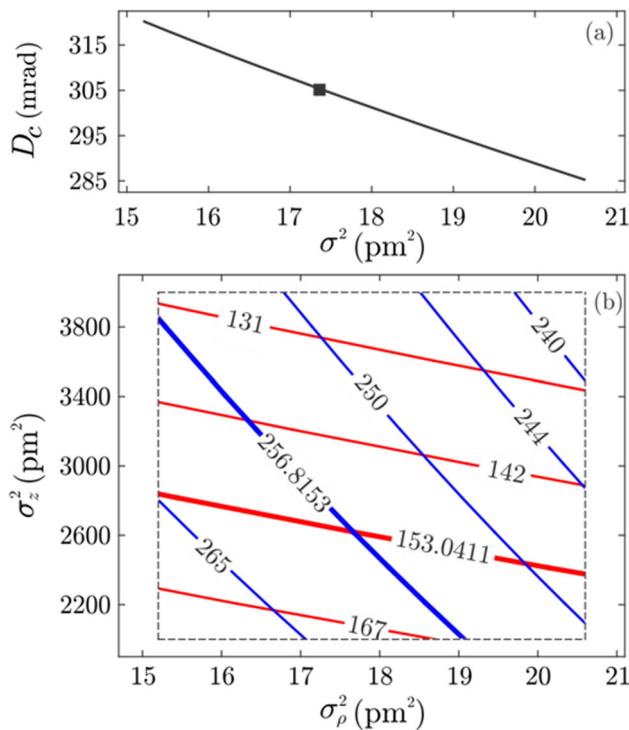


**Fig. 6** **a** Diameter of the outer rainbow as a function of the variance of atomic displacements  $\sigma^2$  in the case of isotropic thermal vibrations of graphene atoms. The black square represents the value of the rainbow  $O'_1$  s diameter shown in Fig. 4a'. **b** Blue lines are contours of the function  $D_c(\sigma_\rho^2, \sigma_z^2)$ , which is the diameter of the outer rainbow generated by the protons transmitted through the graphene sheet in the case of the normal incidence. Red lines are contours of the function  $D_e^m(\sigma_\rho^2, \sigma_z^2)$  representing the minor diameter of the outer rainbow in the tilted graphene sheet by angle  $\Theta = 0.065\pi$  rad. The computation cell is outlined by the black dashed line. Contour values are expressed in mrad. Thicker blue and red lines represent contour levels of the diameters of rainbows  $O'_2$  and  $O''_2$  shown in Fig. 3b', b'', respectively

matrix. Reorientation of the graphene sample transforms the outer rainbow. In turn, this shape evolution can be used to determine the degeneracy of the covariance matrix spectrum [31].

Let us start with the simplest case, the Debye graphene. We observed that the outer rainbow is a circle independent of the graphene orientation. We calculated the diameter of the outer rainbow for different variances in the interval  $[15.20, 20.60]$  pm<sup>2</sup>. Obtained results are presented in Fig. 6a. The minimal considered variance value corresponds to the variance of atomic displacements at the zero temperature. The black square indicates the diameter of the rainbow  $O'_1$  shown in Fig. 4a',  $D_c = 305.27$  mrad. Diameter is a monotonically decreasing function of the variance of atomic vibrations. Hence, Fig. 6a could help determine the unknown variance from the diameter of the corresponding outer rainbow. In the case of the rainbow  $O'_1$

shown in Fig. 4a', the graphically determined variance is  $\sigma^2 = 17.37$  pm<sup>2</sup>.

Covariance in the case of the graphene sheet has two distinct eigenvalues  $\sigma_\rho^2$  and  $\sigma_z^2$ . Therefore, the determination of the unknown variances requires two independent measurements. Here we used information contained in the diameter of the outer rainbow generated in the case of the normal incidence and minor diameter of the outer rainbow in the case of the tilted graphene sheet by the angle  $\Theta = 0.065\pi$  rad, i.e.,  $D_c(\sigma_\rho^2, \sigma_z^2)$ , and  $D_e^m(\sigma_\rho^2, \sigma_z^2)$ , respectively. A system of two equations is obtained:  $D_c = D_c(\sigma_\rho^2, \sigma_z^2)$ , and  $D_e^m = D_e^m(\sigma_\rho^2, \sigma_z^2)$  with unknown variables  $\sigma_\rho^2$  and  $\sigma_z^2$ . The problem can be solved by calculating values of the functions  $D_c(\sigma_\rho^2, \sigma_z^2)$ , and  $D_e^m(\sigma_\rho^2, \sigma_z^2)$  in a specific subset of the two-dimensional parametric space  $(\sigma_\rho^2, \sigma_z^2)$ . We restricted our calculations to the subset  $[15.20, 20.60]$  pm<sup>2</sup>  $\times$   $[2000, 4000]$  pm<sup>2</sup>. Blue and red lines in Fig. 6b are contours of the functions  $D_c(\sigma_\rho^2, \sigma_z^2)$ , and  $D_e^m(\sigma_\rho^2, \sigma_z^2)$  in the selected domain, respectively. Thicker blue and red lines indicate contour levels that correspond to the cases presented in Figs. 4b', b'', respectively. Inside the computational region, each of the functions  $D_c(\sigma_\rho^2, \sigma_z^2)$ , and  $D_e^m(\sigma_\rho^2, \sigma_z^2)$  has exactly one contour of a certain level. Thicker contours cross at the single point. Coordinates of that point are  $(\sigma_\rho^2, \sigma_z^2) = (17.67, 2619.10)$  pm<sup>2</sup>, which are equal to the eigenvalues of the covariance matrix used in the calculation of the corresponding rainbow lines, presented in Figs. 4b', b''. It was shown that a slightly more complicated procedure is required to extract the covariance matrix of atomic vibrations in the case of graphene nanoribbons, where atoms perform totally anisotropic motion [31].

### 4.2 Characterization of graphene point defects

This section will demonstrate how angular yield and the rainbow pattern can be used to determine the type and density of the point defects present in the graphene. To demonstrate the procedure, we confine the analysis to different classes of point defects: vacancy, Stone–Wales, and adatoms defects. A similar analysis could also be used to determine the density of the bridge-like adatom defect. In the perfect graphene case, the rainbow pattern's inner part is a single line, as shown by the insets of Figs. 4a', a'', and a''''. The inner rainbow pattern has a hexagonal symmetry in the normal incidence case. In the analyzed cases of imperfect graphene, none of the obtained patterns poses a hexagonal symmetry. One can quickly notice that rainbow patterns  $I_1$ ,  $I_2$ , and  $I_3$  in Fig. 5a'–c' differ significantly. Patterns  $I_1$  and  $I_3$  share a triangular symmetry, while pattern  $I_2$  does not. On the other hand, patterns  $I_1$  and  $I_3$  differ by the area of angular space they enclose. It was concluded that each defect type produces a distinctive rainbow pattern. Therefore, just by studying the shape of the inner rainbow pattern, one could characterize defect types present in the sample [43].

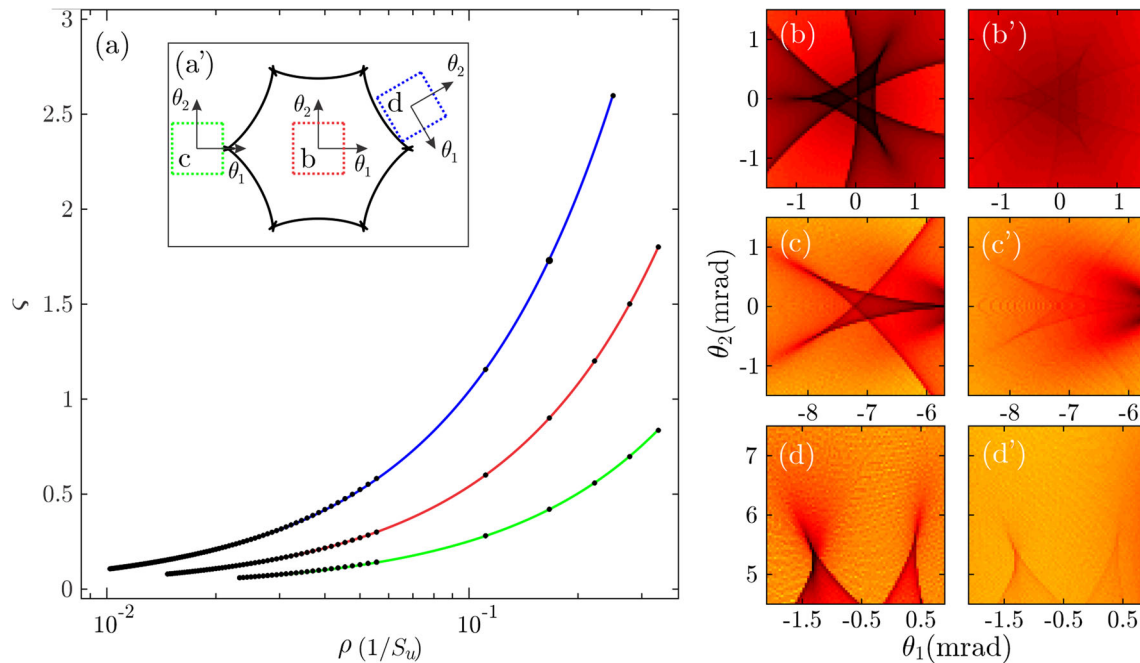


**Fig. 7** **a** Calibration curves for the determination of the unknown densities of defects. Black points show the calculated data points for the vacancy, adatom, and Stone-Wales defects. Red, green, and blue lines show their respective fits. Figure **7a'** shows the inner rainbow pattern of perfect graphene. Relative to it, characteristic regions for the vacancy, adatom, and Stone-Wales defect are outlined by red, green, and blue dashed rectangles, respectively. The angular distributions inside the characteristic rectangles for the maximal defect densities are presented in figures **b–d**, and for the minimal detectable densities of considered defects in figures **b'–d'**

Let us denote the angular distribution of protons transmitted through the perfect graphene by  $Y_0(\theta_x, \theta_y)$ , and by  $Y(\theta_x, \theta_y)$  the angular distribution of protons transmitted through imperfect graphene. The procedure's first step is identifying the scattering angle plane regions in which rainbow patterns  $I_1$ ,  $I_2$ , and  $I_3$  have distinct properties, and the angular yield  $Y_0(\theta_x, \theta_y)$  is featureless. Secondly, we identified subsets of these regions in which rainbow patterns  $I_1$ ,  $I_2$ , and  $I_3$  do not cross each other. The second requirement enables one to consider the contributions of each defect type independently. An identified characteristic region in the case of a vacancy defect is the central triangle enclosed by the cyan dashed line in Fig. 5a'. In the case of Stone–Wales defects, a characteristic segment of the rainbow pattern is formed by two cusped lines inside the dashed cyan rectangle in Fig. 5b'. In the case of the adatoms, the characteristic feature of the rainbow pattern is a large butterfly pattern inside the cyan dashed rectangular line in Fig. 5c'.

Inside each characteristic region, we constructed the regular grid  $\theta_{ij} = \theta_c + i\theta_1 + j\theta_2$ , where  $\theta_1$  and  $\theta_2$  are orthogonal vectors, and  $\theta_c$  is the center of the characteristic region. Corresponding angular yields  $Y(\theta_{ij})$  were calculated using Eq. (10). A quantitative measure of the difference between distributions  $Y_0$  and  $Y$  was introduced by defining the following parameter:

$$\zeta^2(\rho) = \frac{1}{N_1 N_2} \sum_{i=1}^{N_1} \sum_{j=1}^{N_2} \left( 1 - \frac{Y(\theta_{ij})}{Y_0(\theta_{ij})} \right)^2. \quad (17)$$

where  $N_1$  and  $N_2$  are the numbers of grid points in the directions specified by vectors  $\theta_1$  and  $\theta_2$ , respectively. Parameter  $\zeta^2$  is the root-mean-squared relative difference between yields  $Y$  and  $Y_0$  over the characteristic region. Figure 7a' shows the inner rainbow pattern of perfect graphene. Relative to it, characteristic regions for the vacancy, adatom, and Stone–Wales defect are outlined by red, green, and blue dashed rectangles, respectively. The used calculation grid consisted of  $75 \times 75$  points. Black dots in Fig. 7a are calculated  $\zeta^2$  values for different densities of each considered defect type. Densities are expressed in the logarithmic scale. Note that the defined parameter  $\zeta^2$  does not contain information about the shape of the corresponding distribution. Knowledge about the shape of the distribution was already exploited while defining the characteristic regions themselves. If defect density is sufficiently low, contributions to the parameter  $\zeta^2$  that originate from the presence of defects in the graphene lattice may not be distinguishable from the statistical fluctuations and signal noise. Point in the calculations at which the naked eye could not identify a characteristic property of the distribution defined the minimal defect density achievable by this procedure. Angular distributions inside the characteristic regions for the maximal density of vacancies, adatoms, and Stone–Wales defects are presented in Figs. 7b–d, respectively. Corresponding yields in case of the minimal defect densities are presented in Fig. 7b'–d', respectively. Determined minimal defect densities in the case of vacancy, adatom, and Stone–Wales defect type are

0.2730, 0.4318, and 0.1893 nm<sup>-2</sup>, respectively. Notice that minimal detectable densities could be lowered if a human element in the procedure could be superseded. Linear fits of the obtained data points in case of vacancies, Stone–Wales, and adatom defects are presented by red, blue, and solid green lines. The goodness of each performed linear fit is 0.9999. Furthermore, the study [43] demonstrated how a developed procedure could be used to determine the densities of different defect types present in the sample simultaneously.

## 5 Conclusions

We showed that the outer rainbow pattern determines the shape and size of the angular distribution of transmitted protons. A rainbow pattern is generally composed of two parts, the outer and the inner. It was shown that the rainbow pattern's inner part changes with the reorientation of the graphene sample relative to the incident proton beam. However, this change is independent of the covariance matrix  $\Sigma$  of atomic thermal displacements. We showed that outer rainbow lines have an elliptical shape and transform qualitatively the same as the transverse projection of the ellipsoid associated with the inverse of the covariance matrix. These insights proved helpful in building the complete solution to the inverse problem—extraction of the covariance matrix  $\Sigma$  from the size and orientation parameters of the outer rainbow line. We analyzed proton rainbow scattering by imperfect graphene. It was found that the rainbow pattern's inner part differs significantly from the case of perfect graphene. We found that different defect types produce different inner rainbow patterns. Furthermore, we have shown that rainbow patterns and angular distributions of protons transmitted through imperfect graphene could be used to determine the densities of the unknown defects. The developed procedure is applicable even when different defect types are present in the sample simultaneously. In all considered cases, the outer and inner parts of the rainbow pattern do not interact, making simultaneous characterization of both graphene thermal vibrations and graphene crystal structure possible.

**Acknowledgements** Authors acknowledge the support of the Ministry of Science, Technological Development and Innovation of Serbia under the contract No. 451-03-47/2023-01/200017.

## Author contribution

M. H. and M. Č. developed the theoretical framework and performed all calculations. The investigation was supervised by M. Č, and M. H. wrote the first draft of the manuscript.

Both authors commented on the manuscript and approved its final version.

**Data Availability Statement** This manuscript has no associated data or the data will not be deposited. The datasets generated during and/or analyzed during the current study are available from the corresponding author on reasonable request.

## Declarations

**Conflict of interest** The authors declare that they have no known competing financial interests or personal relationships that could have appeared to influence the work reported in this paper.

## References

1. J.A. Venables, G.D.T. Spiller, M. Hanbucken, Nucleation and growth of thin films. *Rep. Prog. Phys.* **47**, 399 (1984). <https://doi.org/10.1088/0034-4885/47/4/002>
2. J.W. Evans, P.A. Thiel, M.C. Bartelt, Morphological evolution during epitaxial thin film growth Formation of 2D islands and 3D mounds. *Surf. Sci. Rep.* **61**(1), 1–128 (2006). <https://doi.org/10.1016/j.surfrep.2005.08.004>
3. K.S. Novoselov et al., Electric field effect in atomically thin carbon films. *Science* **306**(5696), 666–669 (2004). <https://doi.org/10.1126/science.1102896>
4. K. Cao, S. Feng, Y. Han et al., Elastic straining of free-standing monolayer graphene. *Nat. Commun.* **11**, 1 (2020). <https://doi.org/10.1038/s41467-019-14130-0>
5. M.I. Katsnelson, *Graphene: Carbon in Two Dimensions*. Cambridge University Press (2012). <https://doi.org/10.1017/CBO9781139031080>
6. G. Fiori et al., Electronics based on two-dimensional materials. *Nat. Nanotechnol.* **9**, 1063 (2014). <https://doi.org/10.1038/nnano.2014.283>
7. N. Mohanty, V. Berry, Graphene-based single-bacterium resolution biodevice and DNA-transistor: interfacing graphene-derivatives with nano and micro scale biocomponents. *Nano Lett.* **8**(12), 4469–4476 (2008). <https://doi.org/10.1021/nl802412n>
8. T. Yiang et al., Furin-mediated sequential delivery of anticancer cytokine and small-molecule drug shuttled by graphene. *Adv. Mater.* **27**(6), 1021–1028 (2014). <https://doi.org/10.1002/adma.201404498>
9. J.C. Meyer, A.K. Geim, M.I. Katsnelson, K.S. Novoselov, T.J. Booth, S. Roth, The structure of suspended graphene sheets. *Nature* **446**, 7131 (2007). <https://doi.org/10.1038/nature05545>
10. C.S. Allen, E. Liberti, J.S. Kim, Q. Xu, Y. Fan, K. He, A.W. Robertson, H.W. Zandbergen, J.H. Warner, A.I. Kirkland, Temperature dependence of atomic vibrations in mono-layer graphene. *J. Appl. Phys.* **118**, 7 (2015). <https://doi.org/10.1063/1.4928324>
11. A. Fasolino, J.H. Los, M.I. Katsnelson, Intrinsic ripples in graphene. *Nat. Mater.* **6**, 858–861 (2007). <https://doi.org/10.1038/nmat2011>
12. W. Tiao et al., A review on lattice defects in graphene: types, generation. Effects and regulation. *Micromachines* **8**, 5 (2017). <https://doi.org/10.3390/mi8050163>

13. F. Banhart, J. Kotakoski, A.V. Krasheninnikov, Structural defects in graphene. *ACS Nano* **5**(1), 26–41 (2011). <https://doi.org/10.1021/nm102598m>
14. P.T. Araujo, M. Terrones, M.S. Dresselhaus, Defects and impurities in graphene-like materials. *Mater. Today* **15**(3), 98–109 (2012). [https://doi.org/10.1016/S1369-7021\(12\)70045-7](https://doi.org/10.1016/S1369-7021(12)70045-7)
15. J. Jiang et al., Defect Engineering in 2D Materials: Precise Manipulation and Improved Functionalities. *Research* (2019). <https://doi.org/10.34133/2019/4641739>
16. S. Li, M. Liu, X. Qiu, Scanning probe microscopy of topological structure induced electronic states of graphene. *Small Methods* **4**, 3 (2020). <https://doi.org/10.1002/smt.201900683>
17. H.T. Chin et al., Impact of growth rate on graphene lattice-defect formation within a single crystalline domain. *Sci. Rep.* **8**, 4046 (2018). <https://doi.org/10.1038/s41598-018-22512-5>
18. M. Ziatdinov et al., Building and exploring libraries of atomic defects in graphene: scanning transmission electron and scanning tunneling microscopy study. *Sci. Adv.* **5**, 9 (2019). <https://doi.org/10.1126/sciadv.aaw8989>
19. B. Zheng, G.X. Gu, Machine learning-based detection of graphene defects with atomic precision. *Nano-Micro Lett.* **12**, 181 (2020). <https://doi.org/10.1007/s40820-020-00519-w>
20. O.S. Ovchinnikov et al., Detection of defects in atomic-resolution images of materials using cycle analysis. *Struct. Chem. Imaging* **6**, 3 (2020). <https://doi.org/10.1186/s40679-020-00070-x>
21. N. Nešković, Rainbow effect in ion channeling. *Phys. Rev. B* **33**, 6030 (1986)
22. H.F. Krause, S. Datz, P.F. Dittner, J. Gomez del Campo, P.D. Miller, C.D. Moak, N. Nešković, P.L. Pepmiller, Rainbow effect in axial ion channeling. *Phys. Rev. B* **33**, 6036 (1986)
23. S. Petrović, N. Nešković, M. Ćosić, M. Motapothula, M.B.H. Breese, Proton–silicon interaction potential extracted from high-resolution measurements of crystal rainbows. *Nucl. Instrum. Methods Phys. Res. B* **360**, 23–29 (2015)
24. S. Petrović, I. Telečki, D. Borka, N. Nešković, Angular distributions of high energy protons channeled in long (10, 10) single-wall carbon nanotubes. *Nucl. Instrum. Methods Phys. Res. B* **267**(14), 2365–2368 (2009)
25. M. Ćosić, S. Petrović, S. Bellucci, Rainbow channeling of protons in very short carbon nanotubes with aligned stonewales defects. *Nucl. Instrum. Methods Phys. Res. B* **367**, 37–45 (2016)
26. J.F. Ziegler, J.P. Biersack, U. Littmark, *The Stopping and Range of Ions in Solids* (Pergamon Press, New York, 1985). [https://doi.org/10.1007/978-1-4615-8103-1\\_3](https://doi.org/10.1007/978-1-4615-8103-1_3)
27. G. Moliere, Theorie der Streuung schneller geladener Teilchen I: einzelstreuung am abgeschirmten Coulombfeld. *Z. Naturforsch* **2a**, 133–145 (1947)
28. P. Doyle, P. Turner, Relativistic Hartree-Fock X-ray and electron scattering factors. *Acta Cryst. A* **24**, 390–397 (1968). <https://doi.org/10.1107/S0567739468000756>
29. X. Artru, S.P. Fomin, N.F. Shulga, K.A. Ispirian, N.K. Zhevago, Carbon nanotubes and fullerenes in high-energy and X-ray physics. *Phys. Rep.* **412**(2), 89–189 (2005)
30. B.R. Appleton, C. Erginsoy, W.M. Gibson, Channeling effects in the energy loss of 3–11-mev protons in silicon and germanium single crystals. *Phys. Rev.* **161**, 330 (1967). <https://doi.org/10.1103/PhysRev.161.330>
31. M. Ćosić, M. Hadžijojić, S. Petrović, R. Rymzhanov, S. Bellucci, Investigation of the graphene thermal motion by rainbow Scattering. *Carbon* **145**, 161–174 (2019). <https://doi.org/10.1016/j.carbon.2019.01.020>
32. E. Gruber, Ultrafast electronic response of graphene to a strong and localized electric field. *Nat. Commun.* **7**, 13948 (2016). <https://doi.org/10.1038/ncomms13948>
33. L.D. Landau, E.M. Lifshitz, *Mechanics*. Butterworth-Heinemann (1976). <https://doi.org/10.1016/C2009-0-25569-3>
34. S. Petrović, N. Starčević, M. Ćosić, Universal axial (001) rainbow channeling interaction potential. *Nucl. Instr. Methods Phys. Res. B* **447**, 79 (2019). <https://doi.org/10.1016/j.nimb.2019.03.050>
35. N. Starčević, S. Petrović, Crystal rainbow channeling potential for (001) and (111) cubic crystallographic crystals. *Nucl. Instr. Methods Phys. Res. B* **499**, 39–45 (2021). <https://doi.org/10.1016/j.nimb.2021.03.004>
36. M. Ćosić, S. Petrović, N. Nesković, The forward rainbow scattering of low energy protons by a graphene sheet. *Nucl. Instr. Methods Phys. Res. B* **422**, 54 (2018). <https://doi.org/10.1016/j.nimb.2018.02.028>
37. R. Wilhelm, E. Gruber, R. Ritter, R. Heller, S. Facsko, F. Aumayr, Charge exchange and energy loss of slow highly charged ions in 1 nm thick carbon nanomembranes. *Phys. Rev. Lett.* **112**, 153201 (2014). <https://doi.org/10.1103/PhysRevLett.112.153201>
38. D. Jalabert, Real space structural analysis using 3D MEIS spectra from a toroidal electrostatic analyzer with 2D detector. *Nucl. Instrum. Methods Phys. Res. B* **270**, 19 (2012). <https://doi.org/10.1016/j.nimb.2011.09.025>
39. R. Tromp, M. Copel, M. Reuter, M.H. von Hoegen, J. Speidell, R. Koudijs, M.H. von Hoegen, J. Speidell, and R. Koudijs. *Rev. Sci. Instrum.* **62**, 2679 (1991). <https://doi.org/10.1063/1.1142199>
40. R. Tromp, H. Kersten, E. Granneman, F. Saris, Granneman E. F, W. Saris, R.J Koudijs and WJ Kilsdonk. *Nucl. Instrum. Methods Phys. Res. B* **4**, 155 (1984). [https://doi.org/10.1016/0168-583X\(84\)90055-7](https://doi.org/10.1016/0168-583X(84)90055-7)
41. R. Smeenk, H.K.R.M. Tromp, A. Boerboom, F. Saris, *Nucl. Instrum. Methods Phys. Res.* **195**, 581 (1982)
42. M. Ćosić, M. Hadžijojić, S. Petrović, R. Rymzhanov, Morphological study of the rainbow scattering of protons by graphene. *Chaos* **31**, 093115 (2021). <https://doi.org/10.1063/5.0059093>
43. M. Hadžijojić, M. Ćosić, R. Rymzhanov, Morphological analysis of the rainbow patterns created by point defects of graphene. *J. Phys. Chem. C* **125**(38), 21030–21043 (2021). <https://doi.org/10.1021/acs.jpcc.1c05971>

Springer Nature or its licensor (e.g. a society or other partner) holds exclusive rights to this article under a publishing agreement with the author(s) or other rightsholder(s); author self-archiving of the accepted manuscript version of this article is solely governed by the terms of such publishing agreement and applicable law.